

Numerical Simulation of Hypersonic Boundary-Layer Receptivity to Three-Dimensional Wall Perturbations

Xiaowen Wang* and Xiaolin Zhong†
University of California, Los Angeles, California, 90095

The receptivity of a hypersonic boundary layer to three-dimensional wall perturbations is investigated in this paper by numerical simulations. The work is motivated by Tumin's^[1] theoretical analysis on the receptivity of compressible boundary layers to three-dimensional wall perturbations with the help of the biorthogonal eigenfunction system. Specifically, receptivity processes of a Mach 5.92 boundary-layer flow on a flat plate, corresponding to Maslov et al.'s^[2] leading-edge receptivity experiments, to small-scale stationary roughness elements are studied. Due to the fact that the steady base flow profiles are independent of span-wise coordinate, the steady base flow is simulated by solving two-dimensional compressible Navier-Stokes equations with a combination of a fifth-order shock-fitting finite difference method and a second-order TVD scheme. For receptivity simulations, small-scale roughness elements are introduced to the flat plate. The subsequent responses of the hypersonic boundary layer are simulated by solving three-dimensional Navier-Stokes equations with the fifth-order shock-fitting finite difference method. Effect of thermal boundary conditions on the receptivity process is considered by comparing the results of receptivity simulations on adiabatic and isothermal flat plates. The preliminary numerical results show that pressure perturbations are excited inside the boundary layer downstream of the roughness element. In addition, pressure perturbations have relatively large amplitudes near the Mach lines generated by the roughness element. Pressure perturbations can be enhanced by concave roughness element. Counter rotating stream-wise vortices are generated for both cases. However, it is found that roughness element on adiabatic flat plate is more efficient in flow heating and stream-wise vorticity generation. Further studies are currently under way to investigate the receptivity of the hypersonic boundary layer to various wall perturbations.

Nomenclature

\bar{U}	= a vector containing the conservative variables of mass, momentum, and energy
\bar{F}_{ji}	= inviscid flux vectors
\bar{F}_{jv}	= viscous flux vectors
δ_{ij}	= Kronecker Delta function
c_v	= specific heat at constant volume
c_p	= specific heat at constant pressure
τ_{ij}	= elements of viscous stress tensor
μ	= viscosity coefficient
k^*	= heat conductivity coefficient
Re_∞	= unit Reynolds number

* Graduate Student, Mechanical and Aerospace Engineering Department, AIAA Member, xiaowen@seas.ucla.edu.

† Professor, Mechanical and Aerospace Engineering Department, AIAA Associate Fellow, xiaolin@seas.ucla.edu.

I. Introduction

DUE to the fact that a turbulent flow generates much higher shear stress and heat flux to the wall than a laminar flow, the performance and control of hypersonic vehicles are significantly affected by the laminar-turbulent transition of the boundary-layer flows over vehicle surfaces. So the accurate prediction of boundary-layer transition location is very important to the drag calculation and the aerothermal design of hypersonic vehicles.

In order to predict and control boundary-layer transition, extensively studies have been carried out to reveal transition mechanisms. It is found that the paths of boundary-layer flows from laminar to turbulent depend on the environment disturbance level. In an environment of small initial disturbances, the transition of the boundary-layer flow over a smooth surface generally consists of the following three stages:

1. Receptivity process during which small environmental disturbances enter the boundary layer and excite unstable boundary-layer wave modes;
2. Linear development or growth of boundary-layer unstable wave modes which can be obtained by solving the eigen-problem of the homogeneous linearized stability equations;
3. Boundary-layer transition from laminar to turbulent caused by three-dimensional and non-linear effects when the unstable wave modes reach certain amplitudes.

For high level disturbances, the transient growth of boundary-layer waves may directly lead to transition. If the levels of disturbances are even higher, laminar boundary-layer flow can transit to turbulence right after the receptivity process. All these transitions relating to high level disturbances are called bypass transition.

According to the transition mechanisms, it is clearly demonstrated that the study of receptivity process is important because it provides initial conditions of amplitude, frequency, and phase angle for boundary-layer wave modes^[3]. The receptivity process of supersonic and hypersonic boundary-layer flows is more complex than that of subsonic or incompressible flows due to the additional effects of shock wave, compressibility, high temperature, etc. It has motivated extensive theoretical, experimental, and numerical studies of the excitations of boundary-layer wave modes in two-dimensional and three-dimensional high speed boundary layers.

In 1975, Mack^[4] used the compressible linear stability theory (LST) to calculate the amplitude ratio of constant-frequency disturbances for supersonic boundary layers over insulated and cooled-wall flat plate. The objective of his investigation was to determine whether the usage of LST is enough to predict the transition Reynolds number in a supersonic wind tunnel as the free-stream Mach number and wall temperature changed. It was found that the ratio of transition Reynolds numbers in his calculation of the insulated and cooled-wall cases increases much faster than that observed experimentally. The results showed that LST alone is inadequate to determine the transition Reynolds number, and it is necessary to consider the properties of the external disturbances. Choudhari^[5] studied the roughness-induced generation of stationary and nonstationary instability waves in three-dimensional boundary layers over a sweep wing of infinite span. The effects of acoustic-wave orientation and different types of roughness geometries were also considered. Herbert^[6] considered the stability and transition of 3D boundary layers that vary both in stream-wise and span-wise directions with a new approach based on an extension of the parabolized stability equations to 3D boundary layers. The analysis of cross-flow dominated flow showed that the vector of growth rates (α_i, β_i) cannot be solely determined from the local flow characteristics and careful attention must be paid to initial conditions. Fedorov and Khokhlov^[7] studied the receptivity of a hypersonic boundary layer over a flat plate to wall disturbances using a combination of asymptotic method and numerical simulation. They investigated the receptivity mechanisms to different wall disturbances, i.e., wall vibrations, periodic blowing-suctions, and temperature disturbances. It was found that a strong excitation occurs in local regions where forcing disturbances are resonant with boundary-layer wave modes. They also found that hypersonic boundary layers are more sensitive to blowing-suction disturbances than to wall vibrations and temperature disturbances. Forgoston and Tumin^[8] studied a three-dimensional wave packet generated by a local temperature slot in a hypersonic boundary layer. They found that the solution to this initial-value problem can be expanded in a biorthogonal eigen-function system as a sum of discrete and continuous modes. Recently, Tumin^[1] solved the receptivity problem of compressible boundary layers to three-dimensional wall perturbations with the help of the biorthogonal eigenfunction system. In case of receptivity to roughness elements, there are counter rotating stream-wise vortices, streaks at both sides of the hump, and a wake

region downstream from the hump. In supersonic boundary layer, there exist large amplitude perturbations near the Mach waves generated by roughness elements.

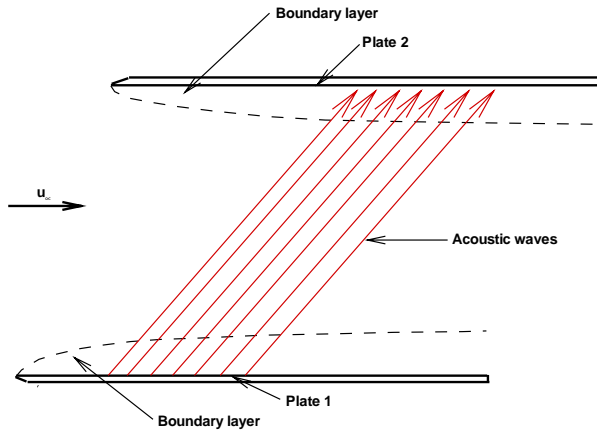


Figure 1. A schematic of the receptivity experiment setup of Maslov and Seminov.

converted into boundary-layer oscillations most efficiently at the leading edge, in the neighborhood of the acoustic branch of the neutral curve, and in the vicinity of lower branch of the neutral curve. Recently, a similar experiment was carried out at a Mach 5.92 flow by Maslov et al. ^[2] to study the leading edge receptivity of the hypersonic boundary layer. It was found that Tollmien-Schlichting waves are generated by the acoustic waves impinging on the leading edge. They also found that the receptivity coefficients depend on wave inclination angles.

Kendall ^[9] experimentally studied the origin and growth of natural fluctuations in zero pressure-gradient boundary layers for several Mach numbers between 1.6 and 8.5. Substantial growths of flow fluctuations were observed within the laminar boundary layer in the early station where the boundary layer is predicted to be stable by LST. These fluctuations were found to be related to the sound field for higher supersonic speeds. The growth rates of these fluctuations in the region downstream of the initial growth are in a reasonable agreement with the LST results of Mack. Maslov and Seminov ^[10] studied the receptivity of a supersonic boundary layer to artificial acoustic waves by utilizing two parallel flat plates as shown in Fig. 1. The acoustic waves generated by an electric discharge system on the lower plate radiated into the external flow and penetrated into the boundary layer of the upper plate as free-stream acoustic disturbances. It was found that the external acoustic waves are

converted into boundary-layer oscillations most efficiently at the leading edge, in the neighborhood of the acoustic branch of the neutral curve, and in the vicinity of lower branch of the neutral curve. Recently, a similar experiment was carried out at a Mach 5.92 flow by Maslov et al. ^[2] to study the leading edge receptivity of the hypersonic boundary layer. It was found that Tollmien-Schlichting waves are generated by the acoustic waves impinging on the leading edge. They also found that the receptivity coefficients depend on wave inclination angles.

With the development of advanced computers and numerical techniques, numerical simulation of the receptivity process by directly solving full Navier-Stokes equations has become a powerful approach. By solving the compressible linearized Navier-Stokes equations, Malik et al. ^[11] investigated the responses of a Mach 8 flow over a sharp wedge of a half-angle of 5.3° to three types of external forcing: a planar free-stream acoustic wave, a narrow acoustic beam enforced on the bow shock near the leading edge, and a blowing-suction slot on the wedge surface. They concluded that these three types of forcing eventually result in the same type of instability waves in the boundary layer. However the receptivity mechanism was not studied in detail. Ma and Zhong ^[12] studied the receptivity mechanisms of the same hypersonic boundary layer to various free-stream disturbances, i.e., fast and slow acoustic waves, vorticity waves, and entropy waves, by solving the two-dimensional Navier-Stokes equations. They found that the stable modes in the boundary layer play a very important role in the receptivity process. Wang and Zhong ^[13, 14] extended Ma and Zhong's work by studying the receptivity mechanisms of the same flow over the sharp wedge to periodic blowing-suction disturbances introduced in a narrow region on the wall. The effects of frequency, location, profile, and length of the blowing-suction actuator on the receptivity process are also investigated based on the numerical simulation results. The numerical results show that mode F, mode S, and acoustic modes are excited by the blowing-suction disturbances. All the modes coexist in the boundary layer just downstream of the forcing region. Far downstream of the forcing region, acoustic modes radiate into the external flow outside the boundary layer. Mode F decays due to its inherent stability while mode S grows substantially because of its instability. As a result, mode S becomes the dominant mode in the boundary layer. It is also found that the excitation of mode S is strongly affected by profile and length of the blowing-suction actuator. All cases of numerical simulations consistently show that the synchronization point of mode F and mode S plays an important role in the excitation of mode S by wall blowing-suction. Mode S is strongly excited when the blowing-suction actuator is located upstream of the synchronization point. On the other hand, when the blowing-suction actuator is downstream of the synchronization point, there is a very weak excitation of mode S, despite the fact that the blowing-suction actuator is still within the unstable region of mode S. A concurrent theoretical study has also been carried out by Tumim, Wang, and Zhong ^[15] to compare the theoretical and numerical results of receptivity coefficients and to analyze the receptivity characteristics. The perturbation flow field downstream of the blowing-

suction actuator is decomposed into boundary-layer wave modes with the help of the biorthogonal eigenfunction system. It was found that there is a good agreement between normal-mode amplitudes calculated with the help of the theoretical receptivity model and those obtained by projecting the numerical results onto the normal modes.

Stemmer et al. ^[16] studied the laminar-turbulent transition mechanisms of a flat plate boundary layer to a harmonic point source disturbances by numerical simulations based on the full Navier-Stokes equations for three-dimensional incompressible flow. The results for early stages agree very well with LST results and with in-flight experiments. Collis and Lele ^[17] numerically investigated the formation of stationary crossflow vortices in a three-dimensional boundary layer due to surface roughness near the leading edge of a swept wing by solving the compressible Navier-Stokes equations. The results showed that convex surface curvature enhances receptivity while non-parallel effects strongly reduce the initial amplitude of stationary crossflow vortices. Zhong ^[18] studied the acoustic receptivity of a hypersonic flow over a parabola by solving full Navier-Stokes equations. It was concluded that the generations of boundary-layer wave modes are mainly due to the interaction of the boundary layer with the transmitted acoustic waves instead of entropy and vorticity waves. In a series of papers, Ma and Zhong ^[19-21] studied the receptivity mechanisms

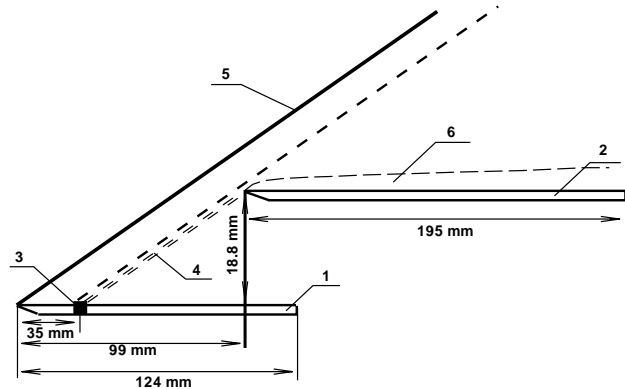


Figure 2. Numerical simulation setup for receptivity of the Mach 5.92 flow to two-dimensional disturbances (1-source plate with 2D perturber, 2-test plate, 3-disturbances actuator, 4-acoustic radiation, 5-bow shock, 6-boundary layer)

of a supersonic boundary layer to various free-stream disturbances by a combination of numerical simulation and linear stability theory. It was found that, in addition to the conventional first and second Mack modes, there exists a family of stable modes which play an important role in the excitation of unstable modes. Dong and Zhong ^[22] carried out parametric simulations of receptivity to freestream disturbances of a Mach 15 flow over 3D blunt leading edges by using high-order shock-fitting finite difference method on parallel clusters. The results showed that the magnitude of transient growth inside the boundary layer also increases by introducing random roughness strips on the wall. For a Mach 10 oxygen flow, Ma and Zhong ^[23] investigated receptivity problems in both perfect gas and thermochemically non-equilibrium gas to consider the real gas effect on receptivity and stability. Compared with the results of perfect gas, the unstable region of non-equilibrium flow is longer and the peak amplitude is higher, which means that the real gas effect destabilizes the boundary-layer modes. Egorov et al. ^[24] developed a numerical algorithm and applied it to the simulation of unsteady two-dimensional flows relevant to receptivity of supersonic and hypersonic boundary layers. For small forcing amplitudes, the second-mode growth rates obtained by numerical simulation agree well with those predicted by the LST with the non-parallel effects. The results of their simulations show a non-linear saturation of fundamental harmonic and rapid growth of higher harmonics. Wang and Zhong ^[25] numerically investigated the steady base flow and the receptivity of the hypersonic boundary layer corresponding to Maslov et al.'s leading-edge receptivity experiments. Figure 2 schematically shows the numerical simulation setup for receptivity to two-dimensional disturbances. The accuracy of the numerical simulation was evaluated by comparing the results of simulations and experiments. The good agreement between the two sets of steady base flows indicated that the numerical simulation of the fifth-order shock-fitting finite difference method was accurate for the hypersonic flow simulation. It was also found that the boundary layer is much more sensitive to blowing-suction disturbances than to wall oscillations and energy perturbations. These results were consistent with those of Fedorov and Khokhlov ^[7].

In this paper, the receptivity of a hypersonic boundary layer to three-dimensional wall perturbations is investigated by numerical simulations. Specifically, receptivity processes of a Mach 5.92 boundary-layer flow on a flat plate, corresponding to Maslov et al.'s ^[2] leading-edge receptivity experiments, to small-scale stationary roughness elements are studied. The work is motivated by Tumin's ^[1] theoretical analysis on the receptivity of

compressible boundary layers to three-dimensional wall perturbations with the help of the biorthogonal eigenfunction system. Due to the fact that the steady base flow profiles are independent of the span-wise coordinate, the steady base flow is simulated by solving two-dimensional compressible Navier-Stokes equations with a combination of a fifth-order shock-fitting finite difference method and a second-order TVD scheme. For receptivity simulations, small-scale roughness elements are introduced to the flat plate. The subsequent responses of the hypersonic boundary layer are simulated by solving three-dimensional Navier-Stokes equations with the fifth-order shock-fitting finite difference method. Effect of thermal boundary conditions on the receptivity process is considered by comparing the results of receptivity simulations on adiabatic and isothermal flat plates.

II. Governing equations and numerical methods

In the current numerical studies, a Mach 5.92 flow over a three-dimensional flat plate as shown in Fig. 3 is considered. The flow is assumed to be thermally and calorically perfect. The governing equations for the simulation are the full compressible Navier-Stokes equations in the conservative form, i.e.,

$$\frac{\partial \bar{U}}{\partial t} + \frac{\partial}{\partial x_1} (\bar{F}_{1i} + \bar{F}_{1v}) + \frac{\partial}{\partial x_2} (\bar{F}_{2i} + \bar{F}_{2v}) + \frac{\partial}{\partial x_3} (\bar{F}_{3i} + \bar{F}_{3v}) = 0 \quad (1)$$

where \bar{U} is a vector containing the conservative variables of mass, momentum and energy, i.e., $\{\rho, \rho u_1, \rho u_2, \rho u_3, e\}$. \bar{F}_{1i} , \bar{F}_{2i} , and \bar{F}_{3i} are inviscid flux vectors, while \bar{F}_{1v} , \bar{F}_{2v} , and \bar{F}_{3v} are viscous flux vectors. The flux vectors can be expressed as

$$\bar{F}_{ji} = \begin{bmatrix} \rho u_j \\ \rho u_1 u_j + p \delta_{1j} \\ \rho u_2 u_j + p \delta_{2j} \\ \rho u_3 u_j + p \delta_{3j} \\ u_j (e + p) \end{bmatrix} \quad (2)$$

$$\bar{F}_{jv} = \begin{bmatrix} 0 \\ \tau_{1j} \\ \tau_{2j} \\ \tau_{3j} \\ -\tau_{1j} u_1 - \tau_{2j} u_2 - \tau_{3j} u_3 - k^* \frac{\partial T}{\partial x_j} \end{bmatrix} \quad (3)$$

with $j \in \{1, 2, 3\}$. In Eq. (2), δ_{ij} ($i = 1, 2, 3$) is the Kronecker Delta function. With the perfect gas assumption, pressure and energy are given by

$$p = \rho RT \quad (4)$$

$$e = \rho c_v T + \frac{\rho}{2} (u_1^2 + u_2^2 + u_3^2) \quad (5)$$

where c_v is the specific heat at constant volume. For compressible Newtonian flow, the viscous stress tensor can be written as:

$$\tau_{ij} = \mu \left(\frac{\partial u_i}{\partial x_j} + \frac{\partial u_j}{\partial x_i} \right) - \frac{2}{3} \mu \frac{\partial u_n}{\partial x_n} \delta_{ij} \quad (6)$$

for $i, j, n \in \{1, 2, 3\}$. In the simulation, the viscosity coefficient, μ , and the heat conductivity coefficient, k^* in Eq. (3), are calculated using the Sutherland's law together with a constant Prandtl number, Pr.

$$\mu(T) = \mu_r \left(\frac{T}{T_r} \right)^{\frac{3}{2}} \frac{T_r + T_s}{T + T_s} \quad (7)$$

$$k^*(T) = \frac{\mu(T)c_p}{\text{Pr}} \quad (8)$$

where $\mu_r = 1.7894 \times 10^{-5} \text{Ns/m}^2$, $T_r = 288.0\text{K}$, $T_s = 110.33\text{K}$, c_p is the specific heat at constant pressure. In this paper, the dimensional flow variables are non-dimensionalized by free-stream parameters. Specifically, density ρ , temperature T , velocities u_1 , u_2 , and u_3 , and pressure p are non-dimensionalized by ρ_∞ , T_∞ , u_∞ , and $\rho_\infty u_\infty^2$. x_1 and x_2 are non-dimensionalized by unit length in meter, while x_3 is non-dimensionalized by the local boundary-layer thickness, $\sqrt{\mu_\infty x_1 / \rho_\infty u_\infty}$. Referring to the coordinate system shown in Fig. 3, x_1 , x_2 , and x_3 are x , y , and z , respectively. The three variables, u_1 , u_2 , and u_3 , are velocities in stream-wise, wall-normal, and span-wise directions, respectively.

The high-order shock-fitting finite difference method of Zhong^[26] is used to solve the three-dimensional Navier-Stokes equations in a domain bounded by the bow shock and the flat plate. In other words, the bow shock is treated as a boundary of the computational domain. The Rankine-Hugoniot relation across the shock and a characteristic compatibility relation coming from downstream flow field are combined to solve the flow variables behind the shock. The shock-fitting method makes it possible for the Navier-Stokes equations to be spatially discretized by high-order finite difference methods. Specifically, a fifth-order upwind scheme is used to discretize the two inviscid flux derivatives of \bar{F}_{1i} and \bar{F}_{2i} . A sixth-order central scheme is used to discretize the two viscous flux derivatives of \bar{F}_{1v} and \bar{F}_{2v} . However, flux vectors of \bar{F}_{3i} and \bar{F}_{3v} in span-wise direction are calculated by Fourier collocation method to achieve high accuracy.

By using the shock-fitting method, the interaction between the bow shock and perturbations induced by roughness elements is solved as a part of solutions with the position and velocity of the shock front being taken as dependent flow variables. A three-stage semi-implicit Runge Kutta method of Zhong et al.^[27] is used for temporal integration. In the leading edge region, there exists a singular point at the tip of the flat plate, which introduces numerical instability when the fifth-order shock-fitting method is used to simulate the flow. Therefore, the computational domain for the shock-fitting simulation starts from a very short distance downstream of the leading edge. A second-order TVD scheme of Zhong and Lee^[28] is used to simulate the steady base flow in a small region including the leading edge to supply inlet conditions for the shock-fitting simulation. For receptivity simulations, small-scale roughness elements are introduced in a downstream region where the shock-fitting method is used. The combination of the shock-fitting method and the TVD method has been validated in cases of supersonic and hypersonic steady flows over a flat plate by Ma and Zhong^[19, 29], and Wang and Zhong^[25].

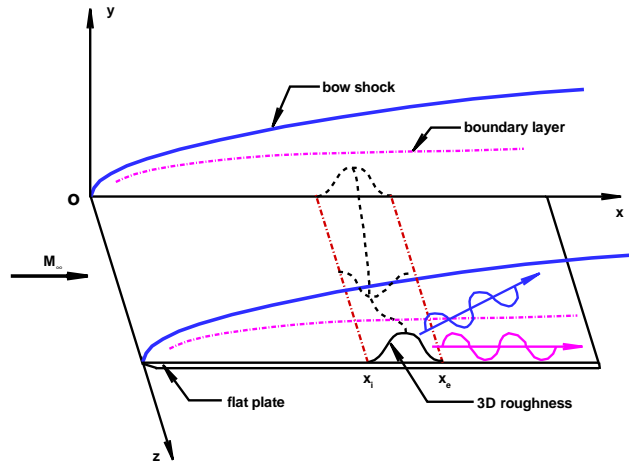


Figure 3. A schematic of the receptivity of the hypersonic boundary layer on a flat plate to roughness elements

The same numerical method has been used by Ma and Zhong in their receptivity studies of supersonic boundary layers over a flat plate and a sharp wedge to various free-stream disturbances ^[19-21]. The good agreement between numerical and LST results indicates that the high-order shock-fitting finite difference method is accurate to simulate the receptivity problems of supersonic boundary layers. The numerical method has also been validated in the theoretical study and comparison with numerical simulation of Tumin, Wang, and Zhong ^[15]. The numerical perturbation field downstream of the blowing-suction actuator is decomposed into boundary-layer wave modes with the help of the biorthogonal eigenfunction system. The filtered-out amplitudes of mode S and mode F agree well with the solutions of the linear receptivity problem. The Fourier collocation method has been tested by Zhong ^[30] to investigate the receptivity of a Mach 6 flow over a flared cone to freestream disturbances. The numerical results are compared with published experiment results. It was found that the steady base flow solutions agree very well with the experiment results. The wave numbers and growth rates of numerical solutions compare reasonably well with the LST results.

III. Flow conditions and roughness element model

The free-stream flow conditions for currently studied flow are the same as those used by Maslov et al. ^[2] in their experiments, i.e.,

$$\begin{aligned} M_\infty &= 5.92 & T_\infty &= 48.69 \text{ K} \\ p_\infty &= 742.76 \text{ Pa} & \text{Pr} &= 0.72 \\ \text{Re}_\infty &= 13 \times 10^6 / \text{m} \end{aligned}$$

The dimensional coordinate, x , can be easily converted to the dimensionless local Reynolds number by

$$\text{Re}_x = \text{Re}_\infty x \quad (9)$$

where Re_∞ is the unit Reynolds number defined as

$$\text{Re}_\infty = \frac{\rho_\infty u_\infty}{\mu_\infty} \quad (10)$$

In linear stability studies of boundary-layer flows, the Reynolds number based on the local length scale of boundary-layer thickness, L , is generally used. They are expressed as

$$R = \frac{\rho_\infty u_\infty L}{\mu_\infty}, \quad L = \sqrt{\frac{\mu_\infty x}{\rho_\infty u_\infty}} \quad (11)$$

Hence, the relation between R and local Reynolds number Re_x is given by

$$R = \sqrt{\text{Re}_x} \quad (12)$$

For the simulation of steady base flow, the wall is adiabatic, and the physical boundary condition of velocity on the flat plate is the non-slip condition. When roughness elements are introduced on the wall, the computational domain and grid structure of receptivity simulation are the same as those of steady simulation due to the fact that the heights of roughness elements are small. Boundary conditions of temperature and velocities on the lowest grid line are specified according to the model of roughness element. Inlet conditions are specified, while high-order extrapolation is used for outlet conditions because the flow is hypersonic at the exit boundary except a small region near the flat plate.

In Dong and Zhong's ^[22] numerical simulations of transient growth in a Mach 15 boundary layer over a blunt leading edge, two types of surface roughness models are introduced. For the first type of surface roughness model, inhomogeneous normal velocity is applied on the surface with the mass conservation being enforced. Components of the randomly distributed small inhomogeneous velocity can be expressed as

$$\begin{cases} u_{wall} = \varepsilon f(x, z)V \sin \theta \\ v_{wall} = \varepsilon f(x, z)V \cos \theta \\ w_{wall} = 0 \end{cases} \quad (13)$$

where ε is the amplitude parameter while V is the inhomogeneous normal velocity. $f(x, z)$ is a random function between $(-1, 1)$ and $\int f(x, z) = 0$ is set to enforce the mass conservation condition. θ is the angle between the tangential direction of the surface and the x axis. According to this model, inhomogeneous normal velocity is directly applied to the wall with roughness. Therefore, the specific roughness geometry needs to be considered in numerical simulations. However, it is hard for numerical simulations to using grid structures attached to the geometries of complex roughness elements.

The second type of surface roughness model is derived with the assumption of small height of the roughness. Due to the existence of roughness elements, the true wall surface changes from $y = 0$ to $y = \varepsilon H(x, z)$, where $H(x, z)$ is a given function. ε is a small parameter to control the height of roughness elements. The physical non-slip conditions of velocity on the true wall are

$$\begin{cases} u(x, \varepsilon H(x, z), z) = 0 \\ v(x, \varepsilon H(x, z), z) = 0 \\ w(x, \varepsilon H(x, z), z) = 0 \end{cases} \quad (14)$$

Temperature boundary conditions on the wall are different for isothermal and adiabatic walls. For small roughness elements, we can do Taylor expansions on boundary conditions, i.e.,

$$u(x, \varepsilon H(x, z), z) = u(x, 0, z) + \left. \frac{\partial u}{\partial y} \right|_{y=0} \varepsilon H(x, z) + O(\varepsilon^2) \quad (15)$$

$$v(x, \varepsilon H(x, z), z) = v(x, 0, z) + \left. \frac{\partial v}{\partial y} \right|_{y=0} \varepsilon H(x, z) + O(\varepsilon^2) \quad (16)$$

$$w(x, \varepsilon H(x, z), z) = w(x, 0, z) + \left. \frac{\partial w}{\partial y} \right|_{y=0} \varepsilon H(x, z) + O(\varepsilon^2) \quad (17)$$

$$T(x, \varepsilon H(x, z), z) = T(x, 0, z) + \left. \frac{\partial T}{\partial y} \right|_{y=0} \varepsilon H(x, z) + O(\varepsilon^2) \quad (18)$$

Substituting Eq. (14) to Eqs. (15)-(17), velocity boundary conditions on $y = 0$ are obtained as:

$$\begin{cases} u(x, 0, z) = -\varepsilon H(x, z) \left. \frac{\partial u}{\partial y} \right|_{y=0} \\ v(x, 0, z) = -\varepsilon H(x, z) \left. \frac{\partial v}{\partial y} \right|_{y=0} \\ w(x, 0, z) = -\varepsilon H(x, z) \left. \frac{\partial w}{\partial y} \right|_{y=0} \end{cases} \quad (19)$$

For the boundary layer over a flat plate as shown in Fig. 3, we have

$$\left. \frac{\partial w}{\partial y} \right|_{y=0} = 0, \quad \left. \frac{\partial v}{\partial y} \right|_{y=0} \ll \left. \frac{\partial u}{\partial y} \right|_{y=0} \quad (20)$$

Therefore, Eq. (19) reduces to

$$u(x, 0, z) = -\varepsilon H(x, z) \left. \frac{\partial u}{\partial y} \right|_{y=0}, \quad v(x, 0, z) = w(x, 0, z) = 0 \quad (21)$$

For this model, the computational domain and grid structure of receptivity simulation can be the same as those of steady simulation, which makes the numerical simulations much easier to investigate the responses of boundary-layer flows to complex of roughness elements. Similar models of roughness elements have also been used by Battaro and Zebib^[31], Collis and Lele^[17], Fedorov and Khokholov^[7].

For the current paper, a model of Eq. (21) is used. The parameters of roughness elements are specified as

$$\varepsilon = 1.0 \times 10^{-4} \quad (22)$$

$$H(x, z) = F(l) \cos \beta z \quad (23)$$

where β is the wave number in span-wise direction, which is given as

$$\beta = \frac{2\pi}{\lambda_z} \quad \text{with} \quad \lambda_z = 6.0 \times 10^{-4} \text{ m} \quad (24)$$

The profile function of roughness elements in stream-wise direction, $F(l)$, can be expressed as

$$\begin{cases} F(l) = 20.25l^5 - 35.4375l^4 + 15.1875l^2 \\ F(l) = F(l)/2.45688 \end{cases} \quad (25)$$

The variable l is a dimensionless coordinate defined within the roughness element ($x_i \leq x \leq x_e$) as

$$l = \begin{cases} 2 \times 0.620287 \times (x - x_i) / (x_e - x_i) & \text{if } x \leq (x_e - x_i) / 2 \\ 2 \times 0.620287 \times (x_e - x) / (x_e - x_i) & \text{if } x \geq (x_e - x_i) / 2 \end{cases} \quad (26)$$

where x_i and x_e are the coordinates of the leading and trailing edges of the roughness element. For the roughness element considered in our simulations, x_i and x_e are equal to 312.25 mm and 316.25 mm, respectively.

In Eq. (25), the constant of 2.45688 is the value of $F(l)$ at the center of the roughness element ($l = 0.620287$), which is used to normalize the profile function. Figure 4 shows the profile function $F(l)$ and the variable l within the roughness element. It is clearly shown that both $F(l)$ and l are symmetric within the roughness region. According to Eq. (21), the positive values of $F(l)$ is equivalent to the negative stream-wise velocity, which indicate that the stream-wise velocity is towards the leading edge of the flat plate. It also shows that the specific 5th-order-polynomial profile function makes the perturbation at the edges smooth.

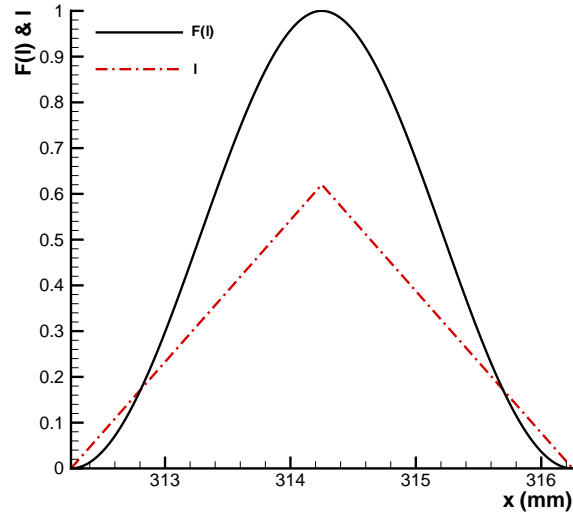


Figure 4. The profile function $F(l)$ and the variable l within the roughness region

IV. Steady base flow

As shown in Fig. 3, steady base flow profiles of the boundary layer over the flat plate are independent of the span-wise coordinate. Therefore, the steady base flow is simulated by solving the two-dimensional compressible Navier-stokes equations with the combination of a fifth-order shock-fitting finite difference method and a second-order

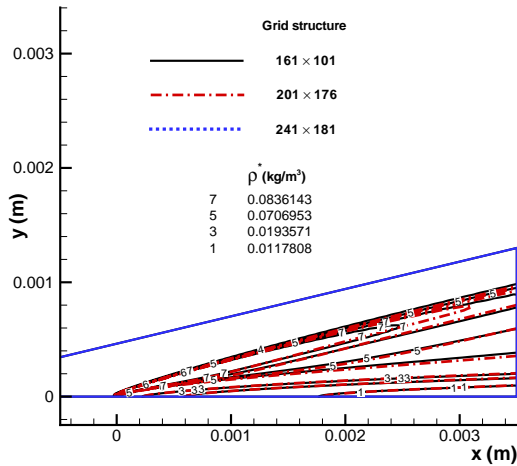


Figure 5. Grid independence check of density contours simulated by TVD scheme based on three sets of grid structures.

refinement studies to ensure the grid independence of the fifth-order shock-fitting simulations.

For the first zone, the inlet conditions are obtained from the results of the second-order TVD method which is used to simulate the steady base flow in a small region including the leading edge. For other zones, inlet conditions are interpolated from the results of the previous zone. The domain for the second-order TVD method starts at $x = -0.0005$ m and ends at $x = 0.0035$ m. Three sets of grid structures are used to check the grid independence of the numerical results. Figure 5 compares the density contours of numerical simulations based on the three sets of grid structures. It shows that the dashdot contours agree well with the dotted contours, while they have discrepancies with the solid contours. This figure indicates that the grid structure (201×176) is enough to ensure grid independence of the results. However, the grid structure (161×101) is too coarse to achieve spatial converged numerical results.

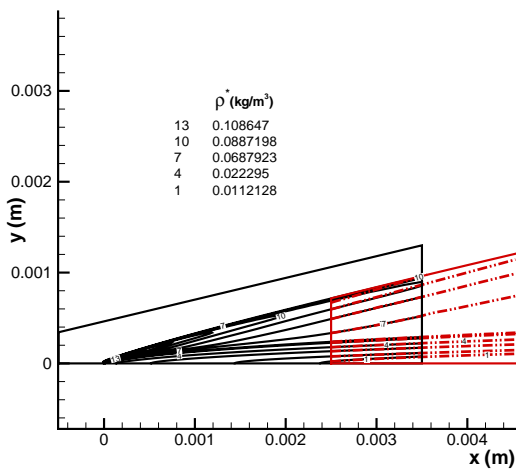


Figure 6. Density contours near the leading edge of the steady base flow on the flat plate obtained by TVD method and shock-fitting method.

TVD scheme. In the leading edge region, there exists a singular point at the tip of the plate, which introduces numerical instability when the fifth-order shock-fitting method is used to simulate the flow. Therefore, the computational domain for the fifth-order shock-fitting method starts at $x = 0.0025$ m and ends at $x = 0.879$ m, corresponding to $R = 180.28$ and $R = 3380.38$, respectively. In actual simulations, the computational domain is divided into 19 zones with a total of 3746 grid points in stream-wise direction. The number of grid points in wall-normal direction is 121 before $x = 0.309$ m and 176 after that location. 41 points are used in the buffering region between two neighboring zones, which has been proved to be sufficient to make the solution accurate and smooth within the whole domain. An exponential stretching function is used in the wall-normal direction to cluster more points inside the boundary layer. On the other hand, the grid points are uniformly distributed in stream-wise direction. The spatial convergence of the results based on this grid structure has been evaluated by grid

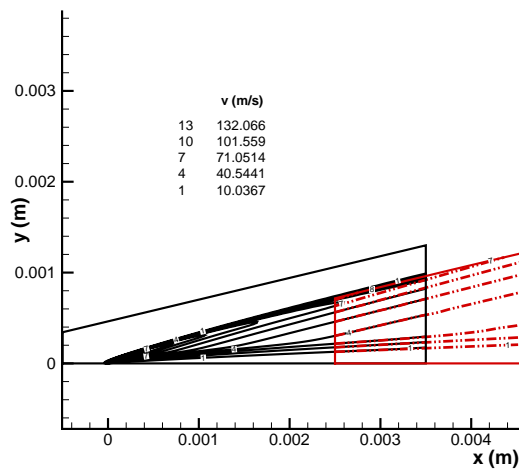


Figure 7. Wall-normal velocity contours near the leading edge of the steady base flow on the flat plate obtained by TVD method and shock-fitting method.

Figures 6 and 7 show the density and wall-normal velocity contours of the steady base flow over the flat plate obtained from the second-order TVD method and the fifth-order shock-fitting method, respectively. The flow field including the leading edge is simulated by the TVD method, while the flow field after $x = 0.0025$ m is simulated by the shock-fitting method. These figures show that density and wall-normal contours have a good agreement near the leading edge of the buffering region, which indicates that the TVD solutions are accurate enough to be used as inlet conditions for the fifth-order shock-fitting simulation in the first zone. The small discrepancies of the contours near the bow shock are due to viscous effect. Because of the viscosity, the bow shock has a finite thickness for TVD simulation, while it is infinitely thin for the shock-fitting simulation. The combination of the shock-fitting method and the TVD method has also been validated in cases of supersonic and hypersonic steady base flows by Ma and Zhong^[29], Wang and Zhong^[14].

Figure 8 shows the pressure contours of the steady base flow over the flat plate simulated by the fifth-order shock-fitting method. The upper boundary of the flow field represents the bow shock induced by the displacement thickness of the boundary layer. A part of the pressure field from $x = 0.03$ m to $x = 0.08$ m is amplified to show clearly the pressure contour within the boundary layer. It is noticed that pressure is almost a constant across the boundary layer and along the Mach lines, which is consistent with the theories of the boundary-layer flow and supersonic aerodynamics. At a fixed location (constant x), the pressure behind the shock is higher than that on the plate due to the existence of the bow shock.

Figure 9 shows the pressure distributions on the flat plate and behind the bow shock versus x . Near the leading edge, there exist great pressure gradients, which are induced by the interaction between the inviscid outer flow and the viscous boundary layer. From upstream to downstream, the inviscid/viscous interaction becomes weaker with the bow shock moves away from the boundary layer. As a result, the pressure approaches a constant value further

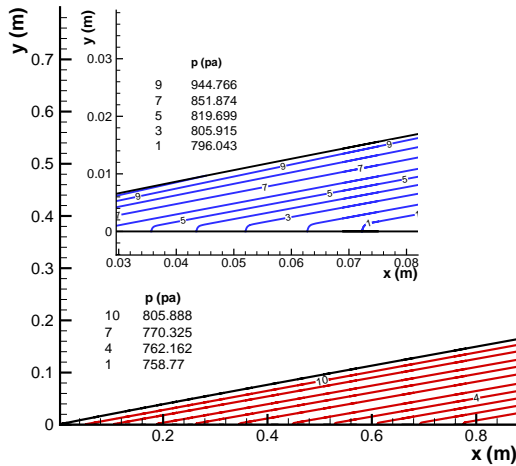


Figure 8. Pressure contours of the steady base flow on the flat plate obtained by the fifth-order shock-fitting finite difference method.

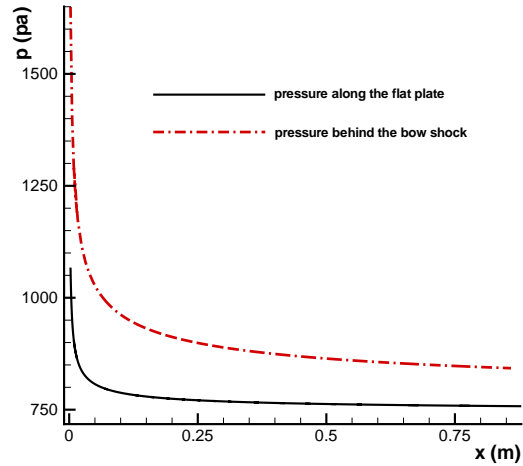


Figure 9. Pressure distributions along the wall and behind the bow shock of the steady base flow obtained by the fifth-order shock-fitting method.

downstream with the pressure gradient decreasing. Again, Fig. 9 shows that the pressure behind the shock is higher than that on the plate at a fixed location (constant x).

More results of the steady base flow over the flat plate can be found in Wang and Zhong's^[25] paper, where the numerical simulated steady flow is compared with that measured by Maslov et al. in their experiments. It was found that the numerical results agree well with the experimental results and the boundary-layer solution near the plate. However, in the region near the edge of the boundary layer, the numerical results have a better agreement with the experimental results. The difference between the numerical results and the boundary-layer solution is mainly caused by the existence of the bow shock, because the effect of the shock is neglected in the calculation of the compressible

boundary-layer equations. Therefore, the effect of the bow shock needs to be considered for supersonic and hypersonic flows.

V. Receptivity simulation results

In order to study the receptivity process of the hypersonic boundary layer to 3D roughness elements on the wall, the two-dimensional steady base flow is firstly extended to three-dimensional base flow according to the fact that base flow is independent of span-wise coordinate. Stationary roughness element modeled by Eqs. (21)-(23) is then enforced on the flat plate in a region from $x_i = 312.25$ mm to $x_e = 316.25$ mm, corresponding to $R = 2014.76$ and $R = 2027.62$, respectively. The subsequent responses of the hypersonic boundary layer are simulated by solving the three-dimensional Navier-Stokes equations with the fifth-order shock-fitting finite difference method. Specifically, a fifth-order upwind scheme is used to discretize the two inviscid flux derivatives of \vec{F}_{1i} and \vec{F}_{2i} . A sixth-order central scheme is used to discretize the two viscous flux derivatives of \vec{F}_{1v} and \vec{F}_{2v} . On the other hand, flux vectors of \vec{F}_{3i} and \vec{F}_{3v} in span-wise direction are calculated by Fourier collocation method to achieve high accuracy. Since there is only one wave mode in span-wise direction, four grid points are enough for Fourier collocation method. The three-dimensional Navier-Stokes equations are solved by the parallel code of Dong and Zhong^[22] on a computer cluster of six nodes. The computation load is uniformly distributed to the six nodes.

Figures 10 and 11 show the pressure contours in span-wise and stream-wise cross-sections of the three-dimensional steady base flow extended from two-dimensional base flow. It is clearly shown in Fig. 10 that pressure contours of the 3D base flow in a cross-section is similar to those of 2D base flow as shown in Fig. 8, i.e., pressure is a constant across the boundary layer and along the Mach lines. Figure 11 clearly shows that pressure is a constant in span-wise direction, because the base flow is independent of the span-wise coordinate. Both Fig. 10 and Fig. 11 show that, at a fixed location (constant x), the pressure behind the shock is higher than that on the plate due to the existence of the bow shock. Figures 10 and 11 indicate that 2D steady base flow is successfully extended to 3D steady base flow.

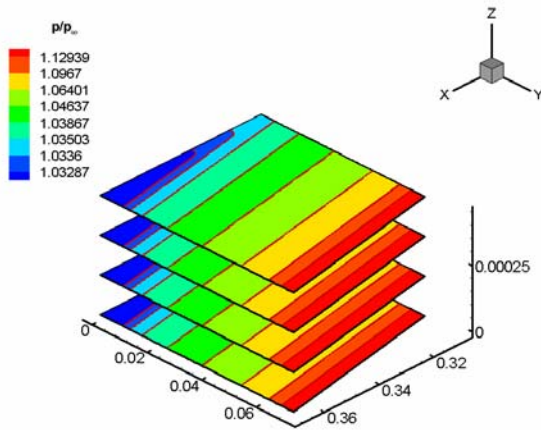


Figure 10. Pressure contours in span-wise cross-sections of the three-dimensional steady base flow extended from two-dimensional base flow.

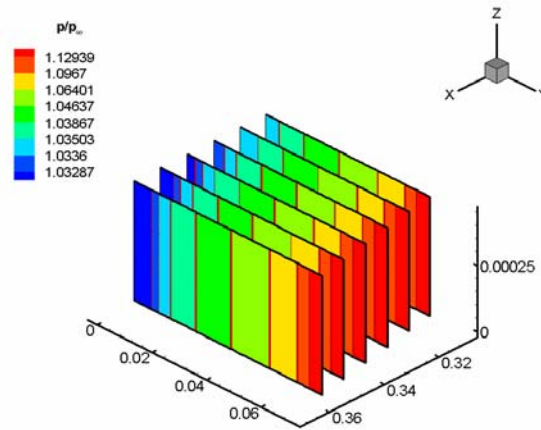


Figure 11. Pressure contours in stream-wise cross-sections of the three-dimensional steady base flow extended from two-dimensional base flow.

Figure 12 shows the contours of stream-wise velocity at the surface of $y = 0$ induced by the 3D stationary roughness element. According to the roughness element model of Eq. (21), convex roughness element induces negative stream-wise velocity while concave roughness element induces positive stream-wise velocity. The contours in Fig. 12 are consistent with the profiles of roughness element in span-wise and stream-wise directions. Figure 13 shows the steam-wise velocity distributions versus x for different span-wise locations at the surface of $y=0$. In the figure, $k = 1, 2, 3,$ or 4 represents the different span-wise locations corresponding to the phase angles of $0, \pi/2, \pi,$ or $3\pi/2$. Again, stream-wise velocity distributions at $k = 1$ and 3 indicate that convex and concave roughness elements induce negative and positive velocities, respectively. It is noticed that no stream-wise velocities are induced at $k = 2$ and 4 , because the heights of roughness element are zero at these two locations.

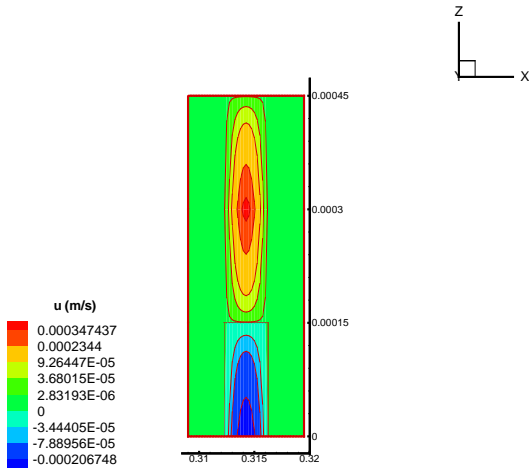


Figure 12. Contours of stream-wise velocity at the surface of $y=0$ induced by 3D stationary roughness element.

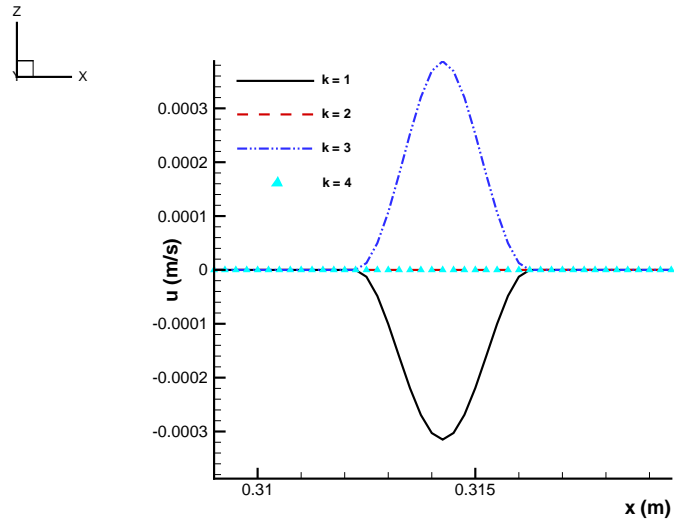


Figure 13. Steam-wise velocity distributions versus x for different span-wise locations at the surface of $y=0$ induced by 3D stationary roughness element.

In current paper, two cases of different wall temperature conditions are simulated to investigate the receptivity process and the effect of thermal boundary conditions on the receptivity process. The perturbation flow field is obtained by subtracting steady base flow from the flow field of receptivity simulation. Specifically, the two cases considered are as follows,

Case 1: Adiabatic boundary condition at $y = 0$

$$\left. \frac{\partial T}{\partial y} \right|_{y=0} = 0 \quad (27)$$

Case 2: Isothermal boundary condition at $y = 0$

For steady base flow simulation, the adiabatic condition is applied on the flat plate. Therefore, the temperature derivative in Eq. (18) is equal to zero, i.e.,

$$T(x, 0, z) = T(x, \varepsilon H(x, z), z) = T_{steady} \quad (28)$$

A. Receptivity to roughness element at adiabatic wall

Figure 14 shows the contours of pressure perturbation at the plane of $k = 1$ induced by 3D stationary roughness element. Downstream of the roughness element, pressure perturbations are excited inside the boundary layer. In addition, pressure perturbations have relatively large amplitudes near the Mach lines generated by the roughness element, which is consistent with Tumin's theoretical analysis [1]. In order to check the three-dimensional properties,

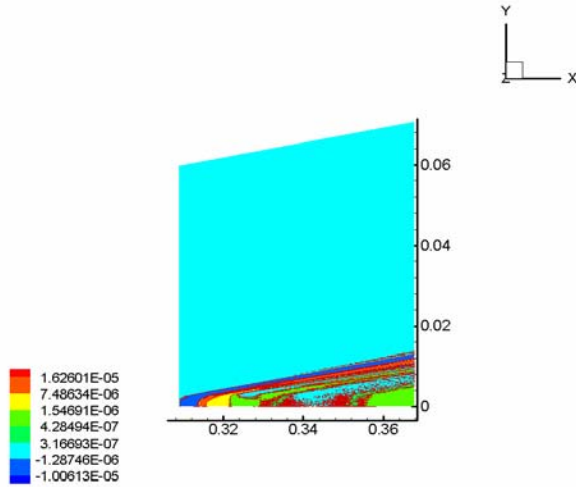


Figure 14. Contours of pressure perturbation at the plane of $k = 1$ induced by 3D stationary roughness element.

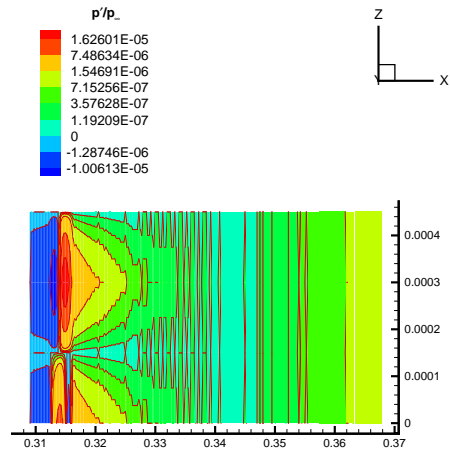


Figure 15. Contours of pressure perturbation at the plane of $y = 0$ induced by 3D stationary roughness element.

contours of pressure perturbation at the plane of $y = 0$ are plotted in Fig. 15. It is noticed that pressure perturbation is negative in the region upstream of the roughness element, while it is positive downstream. Figure 15 also shows that pressure perturbation is periodic with the period of phase angle being π .

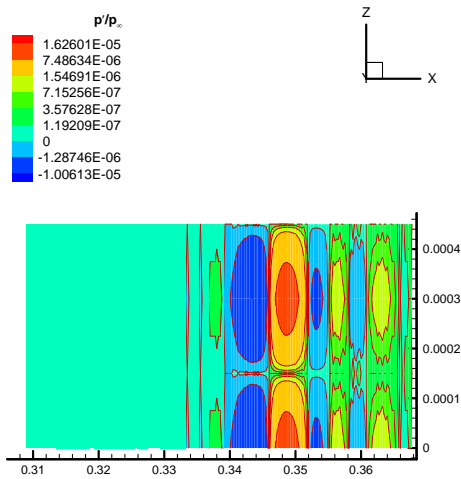


Figure 16. Contours of pressure perturbation at the plane of $j = 88$ induced by 3D stationary roughness element.

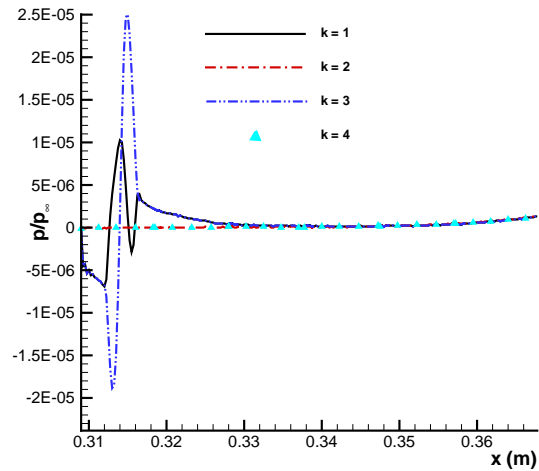


Figure 17. Distributions of pressure perturbation versus x for different span-wise locations at the surface of $y = 0$ induced by roughness element.

Figure 16 shows contours of pressure perturbation at the plane of $j = 88$ (grid line) induced by 3D stationary roughness element. Compared with Fig. 15, it is shown more clearly that pressure perturbation is periodic with the period of phase angle being π , half of the period of roughness element. Figure 17 plots the distributions of pressure perturbation versus x for different span-wise locations at the surface of $y = 0$. Perturbations at $k = 2$ and 4 are small compared with those at $k = 1$ and 3 . Furthermore, pressure perturbation at $k = 3$ is higher than that at $k = 1$. In

order to check the half-periodic properties of pressure perturbation contours and the difference between perturbations at $k = 1$ and 3 as shown in Fig. 17, Fourier transform is applied to decompose the flow field of receptivity simulation in span-wise direction.

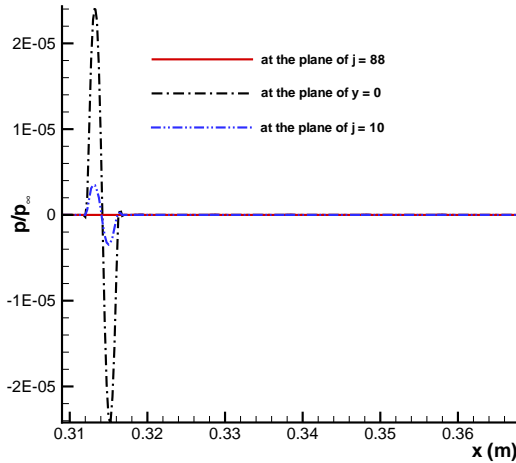


Figure 18. Distributions of perturbation amplitude versus x at the planes of $j = 88, 10$ and $y = 0$ induced by 3D roughness element (period of π).

Figure 18 shows the amplitude distributions of first-mode pressure perturbation at the planes of $j = 88, 10$ (grid lines) and $y = 0$, respectively. It is noticed that the pressure perturbation of the period of π is confined within the forcing region, which indicates that the first-mode perturbation is directly related to the roughness element. The oscillation of perturbation amplitude is caused by the condensation and rarefaction of the flow when it passes the roughness element schematically shown in Fig. 3. For example, at the plane of $k = 1$, the convex element initially condenses the flow and then rarefies the flow, which results in the increase and decrease of perturbation as the dashdot line in Fig. 18. This figure also shows that the amplitude of perturbation decreases with the distance between the considered plane and the flat plate increasing. Perturbation at the plane of $j = 10$ is much lower than that on the plane of $y = 0$. At the plane of $j = 88$ (grid line), no first-mode perturbation is observed because the considered plane exists outside the Mach lines generated by the roughness element. Therefore, the half-periodic property of pressure perturbation contours is more clearly shown in Fig. 16 than in Fig. 15.

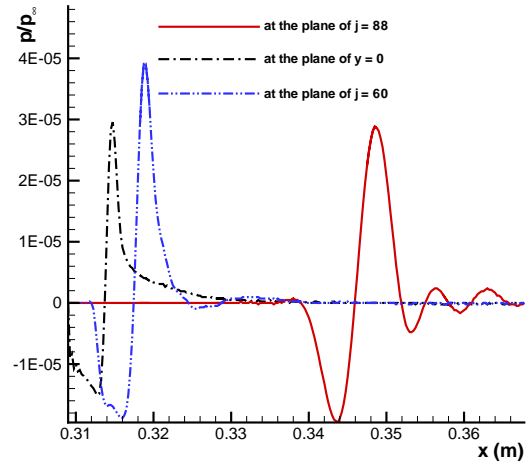


Figure 19. Distributions of perturbation amplitude versus x at the planes of $j = 88, 60$ and $y = 0$ induced by 3D roughness element (period of 2π).

Figure 19 shows the amplitude distributions of second-mode pressure perturbation at the planes of $j = 88, 60$ (grid lines) and $y = 0$, respectively. It is noticed that the pressure perturbation of the period of 2π propagates downstream with the distance between the considered plane and the flat plate increasing. Actually, this is also shown in Fig. 14, because the second-mode pressure perturbation propagates along the Mach lines. The 2π period of perturbation is due to the fact the pressure perturbation is proportional to the square of the stream-wise velocity introduced by roughness element. This figure also shows that the amplitude peak of perturbation initially increases and then decreases with the distance between the considered plane and the flat plate increasing.

At the plane of $k = 1$, the phase angles of first- and second-mode perturbations are zero. Figures 18 and 19 show that amplitudes of the two perturbations have different signs within the forcing region. The combination of the perturbations decreases the total amplitude in forcing region. At the plane of $k = 3$, the phase angles of first- and second-perturbations are π and 2π , respectively. Therefore, amplitudes of the two perturbations have different signs within the forcing region. The combination of the perturbations increases the total amplitude in forcing region. This means that the concave roughness element enhances the pressure perturbation. Outside of the forcing region, first-mode perturbation doesn't exist. Therefore, the total amplitudes of perturbation at the planes of $k = 1$ and $k = 3$ should be the same. All these results are consistently shown in Fig. 19. Figures 18 and 19 also show that the amplitudes of first- and second-mode perturbations have the same order.

Figures 20, 21, and 22 show the perturbation contours of stream-wise, wall-normal, and span-wise velocities in a plane located 2 mm downstream of the roughness element, $x - x_e = 2$ mm. It is noticed that there are no velocity perturbations above the Mach lines generated by roughness element. In Fig. 20, the stream-wise velocity perturbation is negative near the wall, while it is positive near the Mach lines. Such a distribution of stream-wise velocity perturbation results in a positive span-wise vorticity. In Fig. 21, the wall-normal velocity perturbation is positive near the wall, while it is negative near the Mach lines. There exists a surface of zero wall-normal velocity perturbation. In Fig. 22, the span-wise velocity perturbation between surfaces of $k = 1$ and 3 is positive near the wall

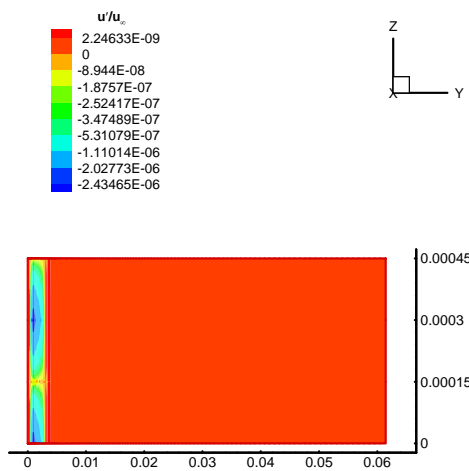


Figure 20. Perturbation contours of stream-wise velocity in a plane located 2 mm downstream of the roughness element (case 1).

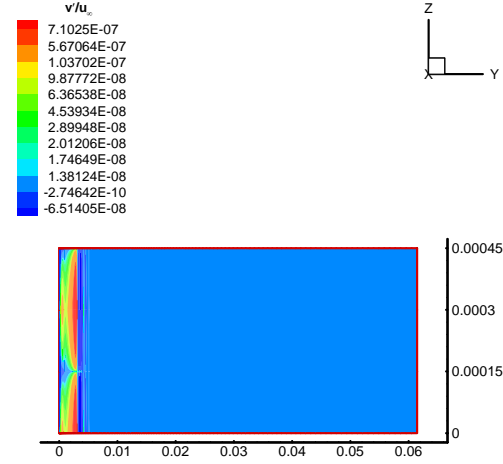


Figure 21. Perturbation contours of wall-normal velocity in a plane located 2 mm downstream of the roughness element (case 1).

and negative near the Mach lines, which results in a positive stream-wise vorticity. However, the span-wise velocity perturbation between surfaces of $k = 3$ and 4 results in a negative stream-wise vorticity. Therefore, counter rotating stream-wise vortices are induced by the roughness element.

Figure 23 shows the perturbation contours of temperature in a plane located 2 mm downstream of the roughness

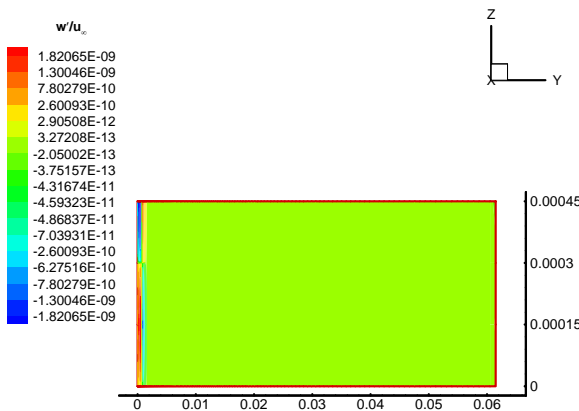


Figure 22. Perturbation contours of span-wise velocity in a plane located 2 mm downstream of the roughness element (case 1).

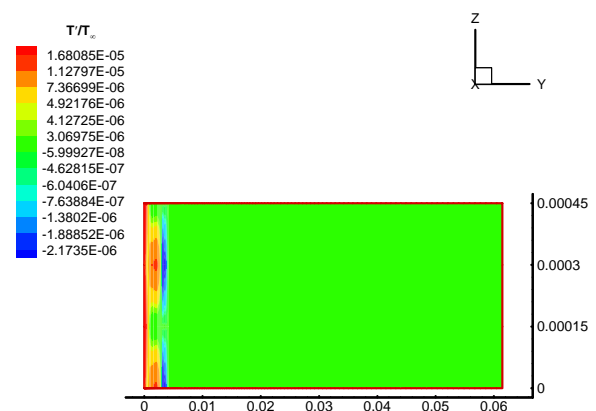


Figure 23. Perturbation contours of temperature in a plane located 2 mm downstream of the stationary roughness element (case 1).

element. There is no temperature perturbation above the Mach lines. It is found that the flow is heated near the wall and cooled near the Mach lines by introducing roughness element on the flat plate. This result is similar to the theoretical analysis of Tumin for a subsonic boundary layer over cooled wall.

B. Receptivity to roughness element at adiabatic wall

When the wall changes from adiabatic to isothermal, similar results can be achieved by receptivity simulation. Downstream of the roughness element, pressure perturbations are excited inside the boundary layer. In addition, pressure perturbations have relatively large amplitudes near the Mach lines generated by the roughness element. In the plane of $y = 0$, pressure perturbation is negative in the region upstream of the roughness element, while it is positive downstream. Perturbations at $k = 2$ and 4 are small. The perturbations at $k = 1$ and 3 have strong oscillations just downstream of the roughness element. Perturbation at $k = 1$ is higher than that at $k = 3$.

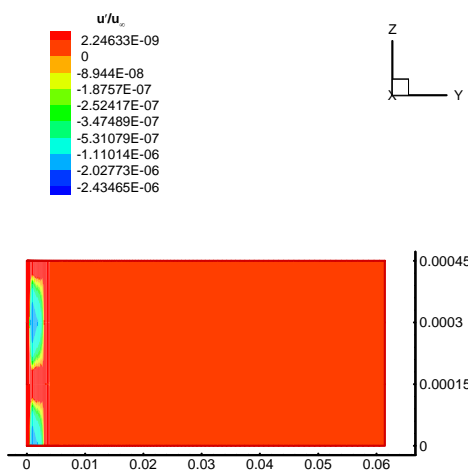


Figure 24. Perturbation contours of stream-wise velocity in a plane located 2 mm downstream of the roughness element (case 2).

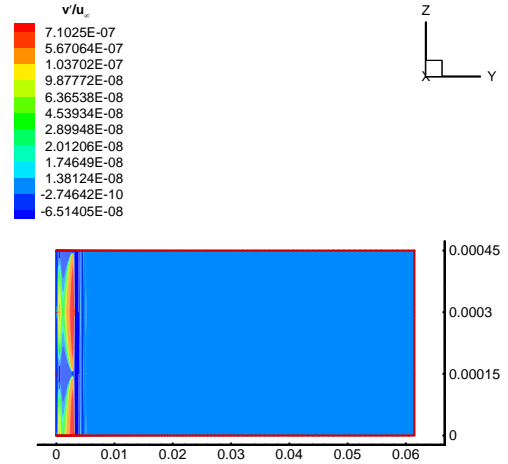


Figure 25. Perturbation contours of wall-normal velocity in a plane located 2 mm downstream of the roughness element (case 2).

Figures 24, 25, and 26 show the perturbation contours of stream-wise, wall-normal, and span-wise velocities in a

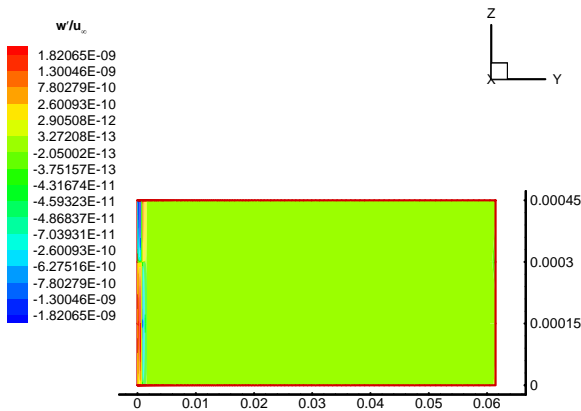


Figure 26. Perturbation contours of span-wise velocity in a plane located 2 mm downstream of the roughness element (case 2).

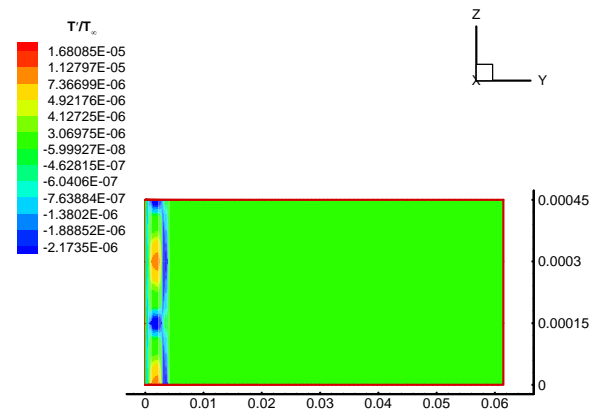


Figure 27. Perturbation contours of temperature in a plane located 2 mm downstream of the stationary roughness element (case 2).

plane 2 mm downstream of the roughness element. Figure 27 shows the perturbation contours of temperature in the plane at the same location. In order to check the effect of wall temperature condition on receptivity, the same levels as those used in Figs. 20-23 are used. Figure 24 shows that the stream-wise velocity perturbation results in a positive span-wise vorticity. Figure 25 shows that the wall-normal velocity perturbation is positive near the wall, while it is negative near the Mach lines. There exists a surface of zero wall-normal velocity perturbation. Figure 26 shows that the span-wise velocity perturbation results in counter rotating stream-wise vortices. Figure 27 indicates that the flow is heated near the wall and cooled near the Mach lines by introducing roughness element on the flat plate.

Compared the numerical results of receptivity process for adiabatic and isothermal walls as shown in Figs. 23 and 27, it is noticed that roughness element on adiabatic flat plate is more efficient in heating the flow near the wall. It can be qualitatively concluded that the velocity perturbations of case 2 is smaller than those of case 1 by comparing Figs. 24-26 with Figs. 20-22, which indicates that roughness element on adiabatic wall is also more efficient in generating stream-wise vortices. In order to show the stream-wise vortices and the effect of wall temperature condition more clearly, Fig. 28 compares velocity vectors in the plane 2 mm downstream of the roughness element for the two cases of adiabatic and isothermal flat plate.

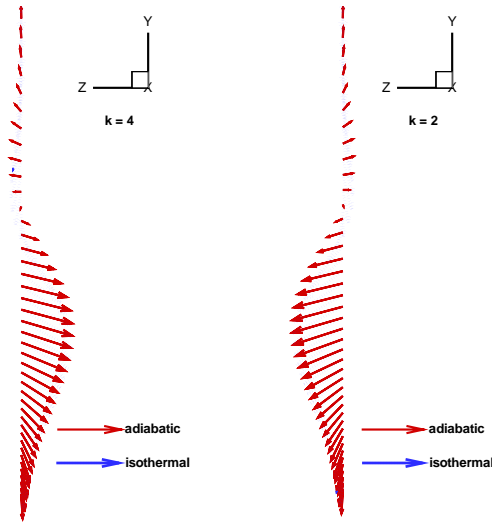


Figure 28. Comparison of velocity vectors in the plane 2 mm downstream of the roughness element for the two cases of adiabatic and isothermal flat plate.

The figure shows that the stream-wise vorticity at the plane of $k = 2$ is positive while it is negative at the plane of $k = 4$. The result is consistent with the Figs. 22 and 26. It is also noticed that the velocity vectors for the case of isothermal flat plate bend to the flat plate much more than those for the case of adiabatic flat plate, which indicates that roughness element on adiabatic wall is more efficient in stream-wise vorticity generation.

VI. Summary

Receptivity processes of a Mach 5.92 boundary-layer flow on a flat plate, corresponding to Maslov et al.'s^[2] leading-edge receptivity experiments, to small-scale stationary roughness elements are studied. Due to the fact that the base flow profiles are independent of the span-wise coordinate, the steady base flow is simulated by solving two-dimensional compressible Navier-Stokes equations with a combination of a fifth-order shock-fitting finite difference method and a second-order TVD scheme. For receptivity simulations, small-scale roughness elements are introduced to the flat plate. The subsequent responses of the hypersonic boundary layer are simulated by solving three-dimensional Navier-Stokes equations with the fifth-order shock-fitting finite difference method. Effect of thermal boundary conditions on the receptivity process is considered by comparing the results of receptivity simulations on adiabatic and isothermal flat plates. The preliminary numerical results show that pressure perturbations are excited inside the boundary layer downstream of the roughness element. In addition, pressure perturbations have relatively large amplitudes near the Mach lines generated by the roughness element. Pressure perturbations can be enhanced by concave roughness element. Counter rotating stream-wise vortices are generated by both cases. However, it is found that roughness element on adiabatic wall is more efficient in flow heating and stream-wise vorticity generation. Further studies are currently under way to investigate the receptivity of the hypersonic boundary layer to various wall perturbations, such as non-stationary roughness elements, periodic blowing-suction disturbances.

Acknowledgments

This work was sponsored by the Air Force Office of Scientific Research, USAF, under AFOSR Grant #FA9550-04-1-0029, monitored by Dr. John Schmisser. The views and conclusions contained herein are those of the authors

and should not be interpreted as necessarily representing the official policies or endorsements either expressed or implied, of the Air Force Office of Scientific Research or the U.S. Government.

References

1. Tumin, A., *Receptivity of Compressible Boundary Layers to Three-Dimensional Wall Perturbations*, in *44th AIAA Aerospace Sciences Meeting and Exhibit*. 2006, AIAA paper 2006-1110.
2. Maslov, A.A., Shplyuk, A. N., Sidorenko, A. A., and Arnal, D., *Leading-edge receptivity of a hypersonic boundary layer on a flat plate*. *Journal of Fluid Mechanics*, 2001. **426**: p. 73-94.
3. Goldstein, M.E., and Hultgren, L. S., *Boundary-layer receptivity to long-wave free-stream disturbances*. *Annual Review of Fluid Mechanics*, 1989. **21**: p. 137-166.
4. Mack, L.M., *Linear Stability Theory and the Problem of Supersonic Boundary-Layer Transition*. *AIAA Journal*, 1975. **13**(3): p. 278-289.
5. Choudhari, M., *Roughness-Induced Generation of Crossflow Vortices in Three-Dimensional Boundary Layers*. *Theoretical and Computational Fluid Dynamics*, 1994. **6**: p. 1-30.
6. Herbert, T., *On the stability of 3D boundary layers*, in *28th AIAA Fluid Dynamics Conference and Exhibit*. 1997, AIAA paper 1997-1961.
7. Fedorov, A.V., and Khokhlov, A. P., *Receptivity of Hypersonic Boundary Layer to Wall Disturbances*. *Theoretical and Computational Fluid Dynamics*, 2002. **15**: p. 231-254.
8. Forgoon, E., and Tumin, A., *Three-Dimensional Wave Packet in a Hypersonic Boundary Layer*, in *43rd AIAA Aerospace Sciences Meeting and Exhibit*. 2005, AIAA paper 2005-0099.
9. Kendall, J.M., *Wind Tunnel Experiments Relating to Supersonic and Hypersonic Boundary-Layer Transition*. *AIAA Journal*, 1975. **13**(3): p. 290-299.
10. Maslov, A.A., and Seminov, N. V., *Excitation of natural oscillations in a boundary layer by an external acoustic field*. *Fluid Dynamics (Historical Archive)*, 1986. **21**: p. 400-404.
11. Malik, M.R., Lin, R. S., and Sengupta, R., *Computation of Hypersonic Boundary-Layer Response to External Disturbances*, in *37th AIAA Aerospace Sciences Meeting and Exhibit 1999*, AIAA paper 1999-0411.
12. Ma, Y., and Zhong, X., *Receptivity to Freestream Disturbances of Mach 8 Flow over A Sharp Wedge*, in *41st AIAA Fluid Dynamics Conference and Exhibit*. 2003, AIAA paper 2003-0788.
13. Wang, X., and Zhong, X., *Receptivity of a supersonic boundary layer over a Sharp Wedge to Wall Blowing/Suction*, in *42nd AIAA Fluid Dynamics Conference and Exhibit*. 2004, AIAA paper 2004-0254.
14. Wang, X., and Zhong, X., *Receptivity of a Mach 8 Flow over a Sharp Wedge to Wall Blowing-Suction*, in *35th AIAA Fluid Dynamics Conference and Exhibit*. 2005, AIAA paper 2005-5025.
15. Tumin, A., Wang, X., and Zhong, X., *Direct Numerical Simulation and the Theory of Receptivity in a Hypersonic Boundary Layer*, in *44th AIAA Aerospace Sciences Meeting and Exhibit*. 2006, AIAA paper 2006-1108.
16. Stemmer, C., Kloker, M. J., and Wagner, S., *DNS of harmonic point source disturbances in an airfoil boundary layer flow*, in *29th AIAA Fluid Dynamics Conference and Exhibit*. 1998, AIAA paper 1998-2436.
17. Collis, S.S., and Lele, S. K., *Receptivity of surface roughness near a swept leading edge*. *Journal of Fluid Mechanics*, 1999. **380**: p. 141-168.
18. Zhong, X., *Receptivity of hypersonic boundary layers to freestream disturbances*, in *38th AIAA Aerospace Sciences Meeting and Exhibit*. 2000, AIAA paper 2000-0531.
19. Ma, Y., and Zhong, X., *Receptivity of a Supersonic Boundary Layer over a Flat Plate. Part 1: Wave Structures and Interactions*. *Journal of Fluid Mechanics*, 2003. **488**: p. 31-78.
20. Ma, Y., and Zhong, X., *Receptivity of a Supersonic Boundary Layer over a Flat plate. Part 2: Receptivity to Freestream Sound*. *Journal of Fluid Mechanics*, 2003. **488**: p. 79-121.
21. Ma, Y., and Zhong, X., *Receptivity of a Supersonic Boundary Layer over a Flat Plate. Part 3: Effects of Different Types of Free-Stream Disturbances*. *Journal of Fluid Mechanics*, 2005. **532**: p. 63-109.
22. Dong, H., and Zhong, X., *Numerical Simulations of Transient Growth in a Mach 15 Boundary Layer over a Blunt Leading Edge*, in *41st AIAA Aerospace Sciences Meeting and Exhibit*. 2003, AIAA paper 2003-1266.
23. Ma, Y., and Zhong, X., *Receptivity to Freestream Disturbances of a Mach 10 Nonequilibrium Reacting Oxygen Flow over a Flat Plate*, in *42th AIAA Aerospace Sciences Meeting and Exhibit*. 2004, AIAA paper 2004-0256.
24. Egorov, I.V., Fedorov, A. V., and Soudakov, V. G., *Direct Numerical Simulation of Unstable Disturbances in Supersonic Boundary Layer*, in *42th AIAA Aerospace Sciences Meeting and Exhibit 2004*, AIAA paper 2004-0588.
25. Wang, X., and Zhong, X., *Numerical Simulation and Experiment Comparison of Leading-Edge Receptivity of A Mach 5.92 Boundary Layer*, in *44th AIAA Aerospace Sciences Meeting and Exhibit*. 2006, AIAA paper 2006-1107.
26. Zhong, X., *High-Order Finite-Difference Schemes for Numerical Simulation of Hypersonic Boundary-Layer Transition*. *Journal of Computational Physics*, 1998. **144**: p. 662-709.
27. Zhong, X., *Additive Semi-Implicit Runge-Kutta Schemes for Computing High-Speed Nonequilibrium Reactive Flows*. *Journal of Computational Physics*, 1996. **128**: p. 19-31.
28. Zhong, X., and Lee, T., *Nonequilibrium real-gas effects on disturbance/bow shock interaction in hypersonic flow past a cylinder*, in *34th AIAA Fluid Dynamics Conference and Exhibit*. 1996, AIAA paper 1996-1856.

29. Ma, Y., and Zhong, X., *Receptivity to Freestream Disturbances of Mach 4.5 Flow over A Flat Plate*, in *40th AIAA Aerospace Sciences Meeting and Exhibit*. 2002, AIAA paper 2002-0140.
30. Zhong, X., *Receptivity of Mach 6 Flow Over a Flared Cone to Freestream Disturbance*, in *42nd AIAA Fluid Dynamics Conference and Exhibit*. 2004, AIAA 2004-0253.
31. Bottaro, A., and Zebib, A., *Gortler Vortices Promoted by Wall Roughness*. *Fluid Dynamics Research*, 1997. **19**: p. 343-362.